Multiport DC-DC conversion incorporating Integrated Magnetics for Renewables

A THESIS
SUBMITTED TO THE FACULTY OF THE GRADUATE SCHOOL
OF THE UNIVERSITY OF MINNESOTA
BY

Suvankar Biswas

IN PARTIAL FULFILLMENT OF THE REQUIREMENTS
FOR THE DEGREE OF
MASTER OF SCIENCE

Professor Ned Mohan

March, 2014

Acknowledgements

This dissertation would be incomplete without the support and contributions of some key people.

Above all, many thanks to my adviser, Professor Ned Mohan, for being a prime motivator, engaging in intense discussions and expressing heartfelt enthusiasm in my ideas even when I myself would be contemplating a dead end. Special thanks to Professor Sairaj Dhople for providing intellectual insight and guiding me with such aplomb. Also, I am indebted to Professor Peter Seiler for agreeing to be part of this committee. His courses were a treat and I borrowed many ideas from them for future research on this project. I would like to thank the Office of Naval Research (ONR) for financial support on this project.

Finally, research cannot be exciting without an enviroment of mutual learning and collaboration. I sincerely want to thank my labmates Ashish, Srikanth, Kartik, Saurabh, Eric, Apurva, John, David, Gysler and Viswesh for being open to answer my questions. I also want to thank my friends in other groups Deepashree, Arja, Sachin and Shailabh for providing me emotional support.

Abstract

Multi-port converter design and analysis presents one of the most intriguing challenges in the incorporation of renewables in the power grid. Choice of topology is of paramount importance to improve the power conditioning. To this effect, the integrated Ćuk topology achieves multiple objectives : low EMI, low component count, simplified MPPT tracking and power management, reduction of filter capacitor requirement, high efficiency. This is achieved by integrating all the magnetic components on a single core, and addition of soft-switching capability thereof. This thesis revisits the concept of integrated magnetics and formulates an elegant solution procedure to the problem of zero-ripple. It investigates the idea of utilizing the concept of a coupled-inductor filter on a three-port converter and removes the need for an external filter, thereby almost introducing an effective DC-DC transformer. The pre-FEM(finite element modelling) selection and design of the core and circuit aspects have been explained in this thesis. The simulation results are presented using PLECS. Additionally, some FEM results are added for the reduced three-winding structure. The validation of some design parameters are also discussed.

A soft-switching scheme has also been demonstrated for a two-port converter with integrated magnetics. This has an active-clamp ZVS turn-on circuit with the addition of a ZCS turn-off. The design of the external components and simulation results for the same are presented as well.

Contents

List of Tables

List of Figures

Chapter 1

Introduction

Multi-functional systems are very much the order of the day. For milliwatt level applications such as smartphones, PDAs, tablets to MegaWatt level systems such as distribution grid, the market increasingly demands compact, intelligent, customizable and energy-efficient plug-and-play devices. For the present problem, we have investigated a novel approach to achieving similar functionality with a multiport DC-DC converter interface at a level of 1 kW. Just as consumer electronics relies heavily on integrated circuits (ICs), a similar approach in principle is employed to integrate passives with a view to reducing the passive requirements, and other features such as low EMI, advanced power management, bidirectional power flow and fast dynamic response. Applications of such a converter are diverse, although primarily intended at interfacing between a renewable energy source (preferably PV with distinct advantages), a standalone or residential distribution grid-tied inverter and a storage port. The converter is not selective of the type of storage, i.e., it can be a Li-ion battery, Fuel Cell or something else.

In this chapter an introduction to multi-port DC-DC conversion is given. This is followed by a discussion on the present state of research in this area, and the scope, outline and contribution of this thesis.

1.1 Multi-port DC-DC conversion

A generalized multi-port converter is shown in Fig 1.1. Salient features of such a converter are the following:

- Bidirectional Power Flow in all ports

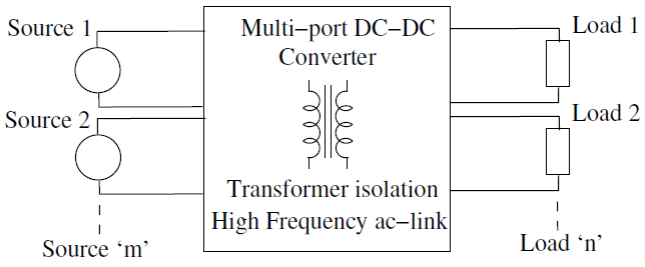

Figure 1.1: Generalized Multiport DC-DC Converter

- Control of Power Flow between the ports as per application requirement
- Port voltages can vary widely
- Galvanic Isolation between all ports
- All ports are interfaced through a high-frequency ac link

Rationale for Integrating Storage With Grid and Renewables

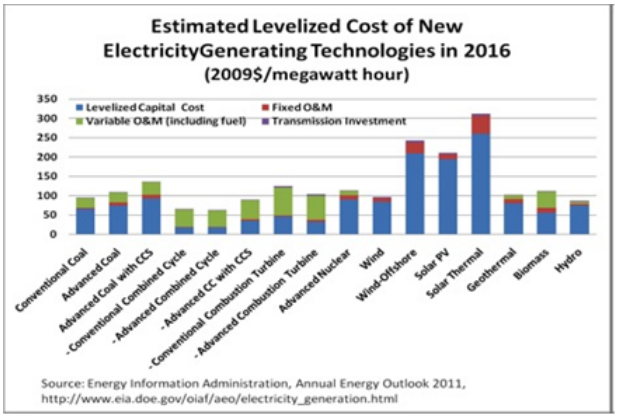

Figure 1.2: Comparative Cost Study of Renewables

The Department of Energy reports that nearly 40 percent of all the energy we consume is first converted to electricity [1]. This percentage would rise to nearly 70 percent if the transportation sector were to be electrified. Solving our energy crisis and reducing our dependence on foreign oil, both of which are tightly coupled to our financial crisis and climate change, would require using renewable resources, such as

solar and wind, and using electricity efficiently. At present, however, using renewable energy is at a crossroad due to falling natural-gas prices; it is projected by DOE that compared to the cost of gas-generated electricity in year 2016 [2], wind-electric to be 150% and PV-based solar to be 300% of the gas-generated electricity , as shown in Fig. 1.2.

Thus, it is becoming difficult to make a business case for renewables [3, 4]. Many utilities have stopped giving special subsidies or have reduced them, and production tax credits from the federal and state governments are highly uncertain [3]. Whats keeping them afloat in near term is Renewable Portfolio Standards (RPS) agreed upon by various states [5]. At the same time, the environmental destruction and climate change is accelerating with reports of arctic ice melting at an amazing speed [6]. This disheartening news can be an opportunity, a call to action, to put more research emphasis to make renewables competitive and to increase the efficiency of how we use electricity through innovative programs and smart grid. In the transportation sector, for example, plug-in vehicles can play a crucial role in reducing the use of fossil fuels and climate change only if electricity is generated by renewable sources [7]. Comparing wind with solar for generating electricity, wind is highly localized and is in places that are far removed from load centers and hence require a robust transmission grid, often nonexistent. Moreover, there seems to be no correlation between the times of high wind speeds to peak load on the utility system. In comparison, solar energy and hence the use of PVs is superior in many respects: 1) it is a very widely distributed resource, and 2) electricity from PVs can be generated very close to load centers, for example at rooftops in residential homes thus does not require an enhanced transmission/distribution grid. However, there still is a time difference between the peak hours of solar irradiance and peak-load on the utility system. As shown in Fig. 1.3, solar irradiance usually peaks between noon and 4:00pm.

These peak hours for solar irradiance do not exactly coincide with the peak load-hours on the utility system. As an example [9], although anecdotal, a local utility co-op has recently agreed to give electric and plug-in car owners a special rate of 6 cents/kWh between the hours of 9:00pm and 8:00am, compared to the general rate of 10 cents/kWh, with the following caveat: the rate for charging car batteries will be 38 cents/kWh between 4:00pm and 9:00pm! Therefore, a time-shift by battery storage of PV-generated electricity by a few hours is needed to supply the battery-stored energy to the utility at a favorable rate. This will also avoid the potential of overloading residential

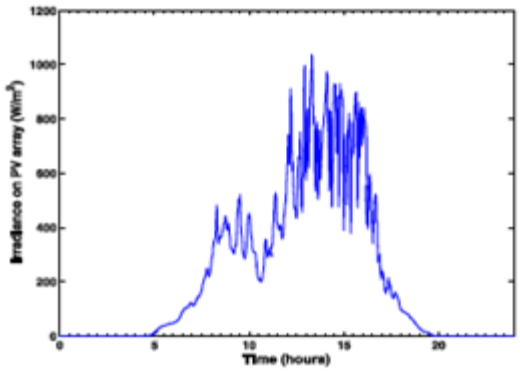

Figure 1.3: Irradiation Levels

distribution transformers if plug-in vehicles become popular.

Making the Case for Battery Storage in combination with PV-Generated Electricity

As shown in Fig. 1, the cost of solar-thermal, or so called Concentrated Solar Power (CSP), is significantly higher than that from PVs. Moreover, CSP is not a possibility in distributed applications such as on rooftops on residential homes. Generating hydrogen and then using it to generate electricity in fuel cells have proven not to be economically feasible for several reasons, including the lack of infrastructure to transport hydrogen where its needed. Therefore, PVs seem to be only way to use solar energy to generate electricity. In PV systems, costs associated with various aspects of the system in getting it installed are considered proprietary. However, it is commonly accepted knowledge that the solar cells, where a great deal of research is focused in universities and national labs, account for only a fraction, such as only one-fifth to one-third, of the cost of the PV systems that ranges from 5 to 6 $/W (peak) installed. Barring a breakthrough in efficiency improvement in solar cells, for example by a factor of two, for the same cost, there is very little possibility for PVs to compete with cheaper alternatives. The only possibility is to couple it with battery storage, as argued earlier, to get a favorable rate.

Additionally, fuel-cell automobiles are considered to be an option for future clean energy automobiles [10]. The primary source will be fuel-cells with the power during acceleration and deceleration supplied from batteries. Fuel-cells have slow dynamic response and hence energy storage is essential in such an application. Batteries can be

charged from fuel-cells and during regenerative braking operation. Three-port converter fits well into this fuel-cell vehicle application. An uninterruptible power supply (UPS) can also be considered as a three-port converter [11].

1.2 State-of-the-Art

Many methods are found in recent literature regarding multi-port conversion, indicating that it is a fairly nascent area. This is proven by the fact that very few OEM (Original Equipment Manufacturer)s actually manufacture such converters. Since they use high-frequency ac link without multiple dc-dc, they have attracted a lot of attention. It is hard to find a tailor-made solution that meets most of the requirements. With this background, we look at a few key topologies that summarize this area.

The outstanding feature of most of these topologies is a boost-type interface, or a bridge topology incorporating soft switching. The converter in [12] has five switches, two coupled inductors and two sets of active clamp circuits; but it has no isolation, which could be a serious drawback in PV systems due to the issue of leakage current. An integrated three-port topology has been proposed in [13], which has interleaved structure on the low-voltage PV port to reduce current ripple to some extent, though not completely eliminate it; also it lacks complete isolation between all the three ports. A novel approach is suggested in [14] utilising a quad-active bridge configuration with the aid of solid-state transformer. This allows bidirectional power flow along with integration of distributed generation, but has many switches and relies on bulky electrolytic dc-link capacitors. References [15, 16] propose full and half-bridge topologies respectively, which are basically two-port structures utilised in a novel way to realise a TPC, but lacks appropriate isolation. A similar topology is encountered in [17], without proper isolation, but it realises four ports using very few components. To conclude this review, we also refer to [18] as being a prototype three-port converter allowing effective power management schemes and soft-switching using series resonant tank circuits.

1.3 Outline and Contributions of the Thesis

1.3.1 Design and Implementation of a Multiport DC-DC Converter incorporating Integrated Magnetics

The proposed converter is shown in Fig.1.4. The main challenge in building the topology is of course, the magnetic core. A step-by-step method of designing the magnetic core is presented, starting with the basic modelling of the magnetic flux path. The converter has six windings on a single EE-core, and the full-fledged analysis of such a structure is strenuous and time-consuming. A trick to convert the structure into a reduced three-winding model is explained. Once that is done, the leakage paths are defined and corresponding inductances explained. The actual physical structure of the core is also proposed. The flux-mmf equations are then defined, and analyzed to yield a zero-ripple condition for all three terminals. This analysis incorporates a duality transformation between the circuit (inductance) model and the actual flux-reluctance (physical) model. Apart from this, the other design equations, i.e., the flux saturation conditions, and maximum allowable ripple on the center winding are also defined. The core is designed for the case when all the three-ports are online, and some investigation on how this converter operates when the PV port is offline, is also presented.

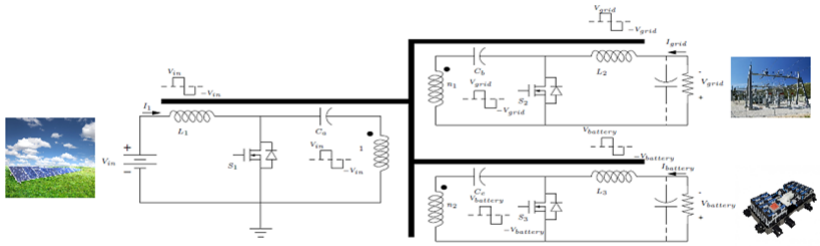

Figure 1.4: Three-Port Bidirectional Converter

1.3.2 Design and Implementation of a Novel Soft-Switching Scheme for a two-port Ćuk converter with Integrated Magnetics

The proposed topology is shown in Fig.1.5. A key objective is to investigate the tradeoff due to addition of snubber and soft-switching components against the basic design

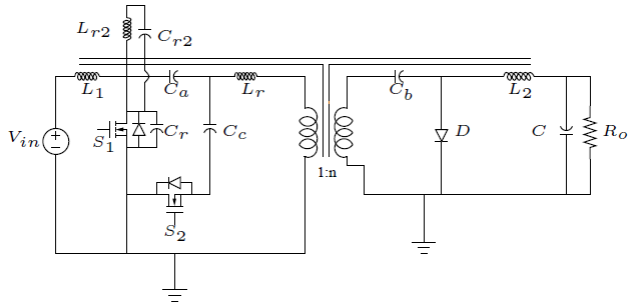

Figure 1.5: Two-Port Integrated Magnetic Topology with Soft-Switching

of integrated magnetic components. Similar to the three-port converter, a step-by-step design procedure for the design of the magnetics is explained, following the same general ideas as before. The motivation of adding the soft-switching components is then explained. The active-clamp circuit with the addition of a switch and clamp capacitor achieves the ZVS turn of both the primary side switches. The passive snubber branch with the extra inductor and capacitor add a ZCS turn-off of the primary side switches. The various stages in the soft-switching process are explained. The design considerations for all these components are explained from a nominal set of specs: power, voltage conversion ratio, and nominal duty-ratio. Finally, the trade-offs due to addition of these extra components on the zero-ripple condition is then presented.

Chapter 2

Integrated Magnetics

2.1 Motivation and Rationale

The basic principle of a two-winding transformer is : An ac voltage waveform on the primary winding induces a proportional voltage waveform on the secondary winding, on account of the same flux flowing in the core. The cause-and-effect can be reversed, i.e., when the voltage waveforms on two magnetic devices are the same, they can be coupled on to a single magnetic core as demonstrated in Fig.2.1. The advantages are twofold : size and weight reduction, as well as performance improvement, as will be demonstrated.

For example, consider the separate inductor windings in Figure 2.1. The positive polarity terminals on each winding are marked with a dot. We have

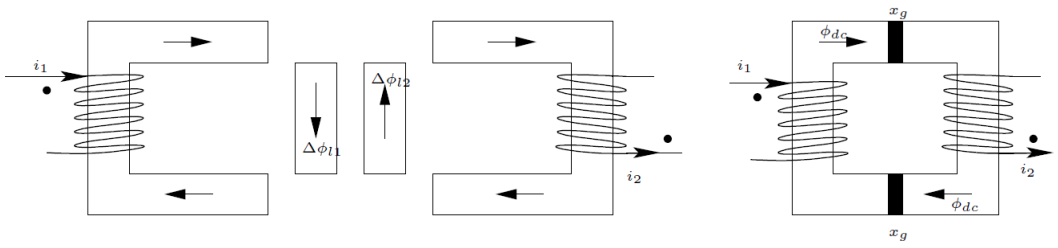

Figure 2.1: (a) Separate Inductors (b) Coupled Inductor Structure

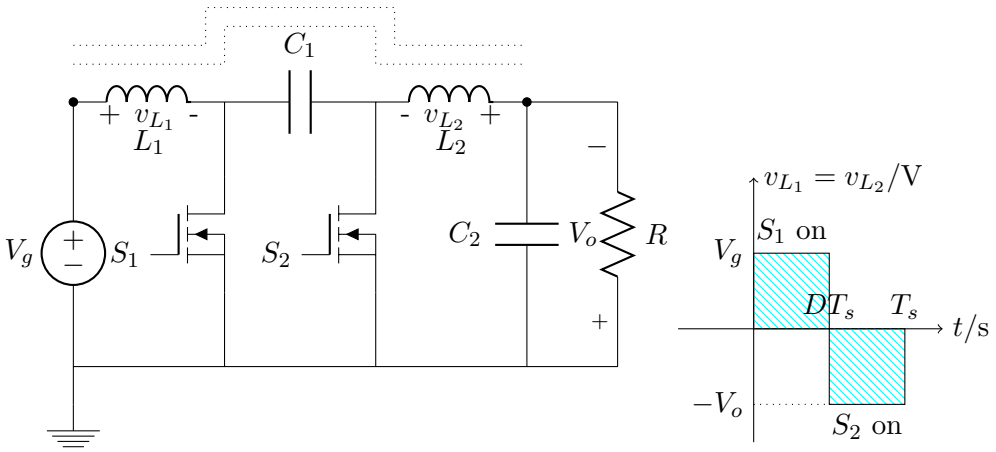

Figure 2.2: Basic Ćuk converter

$$\int v_{L_1} dt = \int v_{L_2} dt \tag{2.1}$$

$$\Delta\phi_{l_1} = \Delta\phi_{l_2} \tag{2.2}$$

Hence no ac flux flows through the center branch and it can be eliminated. The dc fluxes add up, according to the principle of superposition. However, the air-gap needs to be increased in order to maintain this linearity.

For the basic Ćuk converter, it has this fortunate property of identical voltage waveforms across the inductors. Hence the total ac flux in the center branch (in Fig.2.1) is zero, and can be removed. This leads to a smaller, lighter magnetic component but with the same power density. This directly leads to removal of additional core losses, thereby increasing efficiency.

Magnetic Scaling Law

For a transformer, or coupled inductor with identical voltage waveforms, the maximum voltages that can be supported without saturation on the primary and secondary windings are :

$$V_1 = 4N_1 B_{max} S f_s \tag{2.3}$$

$$V_2 = 4N_2 B_{max} S f_s \tag{2.4}$$

where B_{max}=max. flux density in the core, S= cross-section, and N_1 and N_2 are the turns of each winding. Also the window area is fully utilized when

$$kW = \frac{N_1 I_1 + N_2 I_2}{J} \tag{2.5}$$

where k is the empirical fill factor of the windings, and J the current density, usually about 2-4 A/mm^2. Hence the power handling capacity of the magnetic structure is given by

$$P = VI \propto kWS \propto l^4 \Rightarrow V(vol.) \propto P^{3/4} \tag{2.6}$$

It is clear that the volume/weight of a magnetic device as a function of the linear dimension (l) goes up slower than the power handling capacity. Therefore, significant increase in power density can be obtained by integrating the magnetics structure. Apart from this, special converters (like Ćuk) with identical voltage waveforms can have the additional advantage of the ripple-steering effect, as explained in the next section.

2.2 Ripple-Steering Phenomenon

This is a very general result and can be applied to all switching converters where the coupled inductor technique can be practiced to advantage. This is an ac phenomenon and works even under no-load condition, barring non-idealities. For a 2-winding inductor, we have the following equations:

$$v_1 = L_{11}\frac{di_1}{dt} + L_M \frac{di_2}{dt} \tag{2.7}$$

$$v_2 = L_M \frac{di_1}{dt} + L_{22}\frac{di_2}{dt} \tag{2.8}$$

The equations can be rearranged as

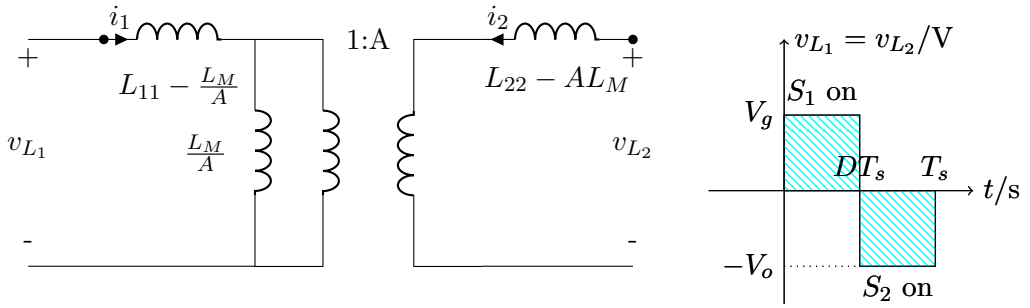

Figure 2.3: T-model of Coupled Inductor

$$v_1 = (L_{11} - \frac{L_M}{A})\frac{di_1}{dt} + \frac{L_M}{A}\frac{d}{dt}(i_1 + Ai_2) \tag{2.9}$$

$$v_2 = (L_{22} - AL_M)\frac{di_2}{dt} + AL_M\frac{d}{dt}(\frac{i_1}{A} + i_2) \tag{2.10}$$

Equations(2.9) and (2.10) mean the coupled inductor can be represented as the following 2-winding transformer (Fig.2.3).

In order to have zero ripple current for the second winding, $\frac{di_2}{dt} = 0$. This happens when the voltage across $L_{22} - AL_M$ is zero. Solving the circuit (Fig 2.3) gives

$$L_{11} = L_M \tag{2.11}$$

$$\Rightarrow n = k \tag{2.12}$$

where $n = \sqrt{L_{11}/L_{22}}$, $k = \frac{L_M}{\sqrt{L_{11}L_{22}}}$ (coupling coefficient)

This would lead to shifting of all the ripple on Winding 2 to winding 1. However, if we want to have zero-ripple on both the windings, we would need a third winding with proportional voltage waveforms. This is accomplished by the following variant of the Basic Ćuk Converter (Fig.2.4).

The same inductance matrix approach as in the 2-winding case can be a candidate here for deriving the zero-ripple condition.

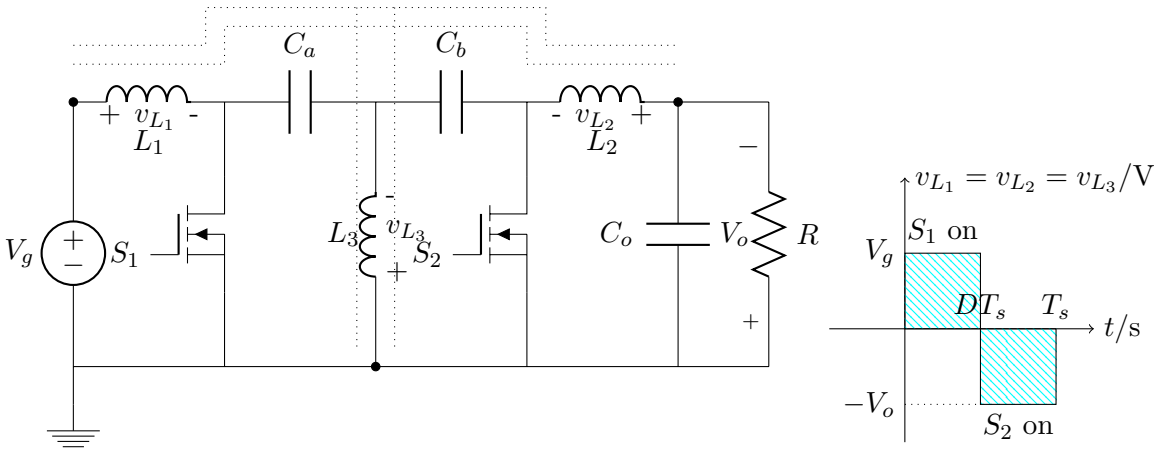

Figure 2.4: 3-Winding Coupled Inductor

$$\begin{bmatrix} v_1 \\ v_2 \\ v_3 \end{bmatrix} = \begin{bmatrix} M_{11} & M_{12} & M_{13} \\ M_{21} & M_{22} & M_{23} \\ M_{31} & M_{32} & M_{33} \end{bmatrix} \begin{bmatrix} \dot{i}_1 \\ \dot{i}_2 \\ \dot{i}_3 \end{bmatrix}$$

where $M_{ii} = L_i$ the self inductance of winding i and $M_{ij} = k_{ij}\sqrt{L_i L_j}$ is the mutual inductance between i and j. Doing a similar kind of analysis from the two winding structure, we get the following conditions for zero-ripple for windings 1 and 2:

$$M_{23}{}^2 = M_{33}M_{22} \tag{2.13}$$
$$M_{21}M_{32} = M_{23}M_{31} \tag{2.14}$$
$$M_{21}M_{32} = M_{22}M_{31} \tag{2.15}$$
$$M_{11}M_{33} = M_{13}M_{31} \tag{2.16}$$
$$M_{11}M_{32} = M_{12}M_{31} \tag{2.17}$$

The conditions are too many and this is a formidable challenge to solve. We note the following :

- No. of equations for the zero-ripple condition increases combinatorially with the no. of windings.
- The equations hardly represent the actual physical magnetic structure and hence

offer very little tips for the magnetic design. This is true even for the two-winding case.

- Apart from this, we have the following for a 2-winding structure :

$$\begin{bmatrix} v_1 \\ v_2 \end{bmatrix} = \begin{bmatrix} M_{11} & M_{12} \\ M_{21} & M_{22} \end{bmatrix} \begin{bmatrix} \dot{i_1} \\ \dot{i_2} \end{bmatrix}$$

In this case,

$$v_{1_{|v_2=0}} = l_1 \frac{di_1}{dt} \tag{2.18}$$

$$\Rightarrow \frac{\Delta l_1}{l_1} = \frac{2k^2}{1-k^2} \frac{\Delta k}{k} \tag{2.19}$$

For tight coupling, i.e, $k = 0.98$, if $\frac{\Delta k}{k} = 1\% \Rightarrow \frac{\Delta l_1}{l_1} = 48.5\%$!!! This shows that the general inductance model is ill-suited for computations at tight coupling, especially in evaluating the dynamic response.

From the above considerations, it is evident that we need a more physical design approach for designing the zero-ripple bidirectional Ćuk Converter, discussed in the next chapter.

Chapter 3

Three-Port Converter Design

3.1 Objectives Addressed

This paper addresses the following objectives for a TPC(Three-Port Converter): high efficiency, zero-ripple terminal currents, low component count, by effectively utilizing a special feature of the Ćuk converter (as explained in Section II) to achieve reduction in weight, plug-and-play capability and effective control. This is done by integrating the inductor and transformers onto a single magnetic core. The resulting magnetic circuit is then analyzed to generate a zero-ripple current on all the input and output ports, which is a requirement for an interfacing converter many manufacturers would approve. In addition to reducing issues with electromagnetic interference (EMI), it also removes the need for a high-bandwidth controller and a dc-link capacitor at the PV input due to dc currents being drawn from the PV source.

This converter is suitable for hybridizing several sources/loads for widely different nominal voltages. Supplying the output load, charging or discharging the battery can be made by the PV source. It also enables the charging of a plug-in hybrid vehicle at the storage port.

3.2 Some Background on the Ćuk Converter

Unlike most of the other DC-DC topologies, the Ćuk converter provides continuous current at its input and output terminals. However, as described in [22], it has the additional property that the switching voltage waveforms across its input and output inductors are identical. This presented an opportunity to couple the inductors on a

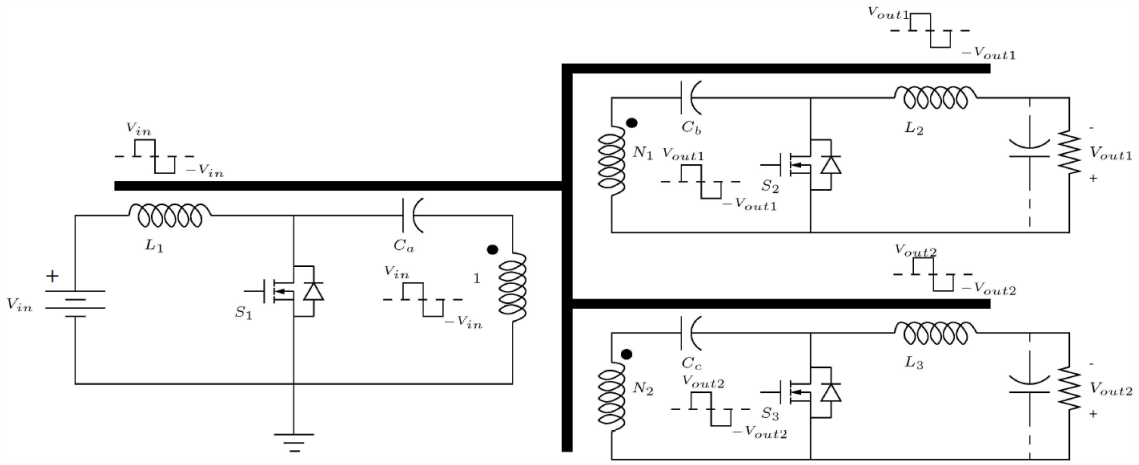

Figure 3.1: Three Port Bidirectional Ćuk Converter

single magnetic core. A further improvement was outlined in [22] whereby isolation of the input and output terminals was proposed and all the switching current ripple from the input and output inductors. This is on account of the fact that the voltage waveforms across all the magnetic components still remained proportional. The same property has been found to be true for the three-port case(Fig.3.l). Advantage has been taken of this fact, as will be outlined in Section III. The idea of a three-port converter was also touched upon in [22] but lacked appropriate analytical considerations. Also it was unidirectional and envisaged nonplanar magnetics (along with gapped cores), which made the actual design considerably more difficult.

In this thesis, we have tried to formulate an elegant way of solving the zero-ripple problem for a three-port Cuk converter. Instead of having a three-dimensional core structure [22], we have simply used the fact that windings around a single leg of the core will have proportional voltages. Initially, a two port converter was designed with appropriate current ratings. The three-port turns ratios were then chosen so that effective current seen by the primary side was the same as in the two port case. This is further explained in Section III.

3.3 Design Methodology

3.3.1 Scaling to Primary

The design begins with the scaling of the output terminals to the primary side(Fig.3.2). As outlined in [29], the equivalent pi-model for the three-winding transformer is uniquely determined, whereas for a two-winding one it is overdetermined, and for four, it only works under additional assumptions.

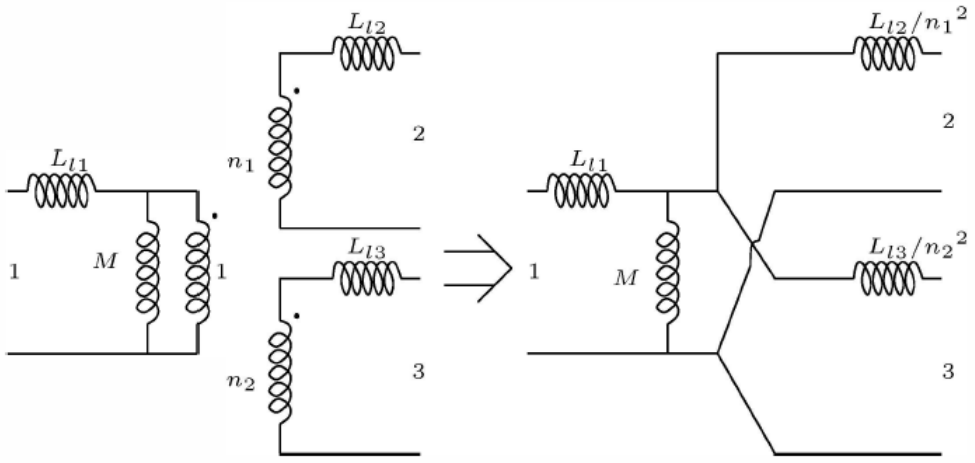

Figure 3.2: Scaling to Primary

3.3.2 Leakage Parameter Characterization

An EE-core is chosen for this kind of application because of its inherent symmetry with respect to leakage issues. The flux distribution in each of the outer legs is symmetrical around the air-gap, hence both side-by-side windings will produce the same voltage as a single full length winding [26]. The following assumptions are then made with respect to the EE-core (Fig.3.3) :

- The leakage on the outer legs is assumed to be neglible.
- The leakage flux path on the center leg can be described by an additional core leg (with air-gap length l).

This leakage parameter is described by the equation (3.1) where μ_0 is the permeability of free space, S is the cross-sectional area of the center leg and R_l is the leakage

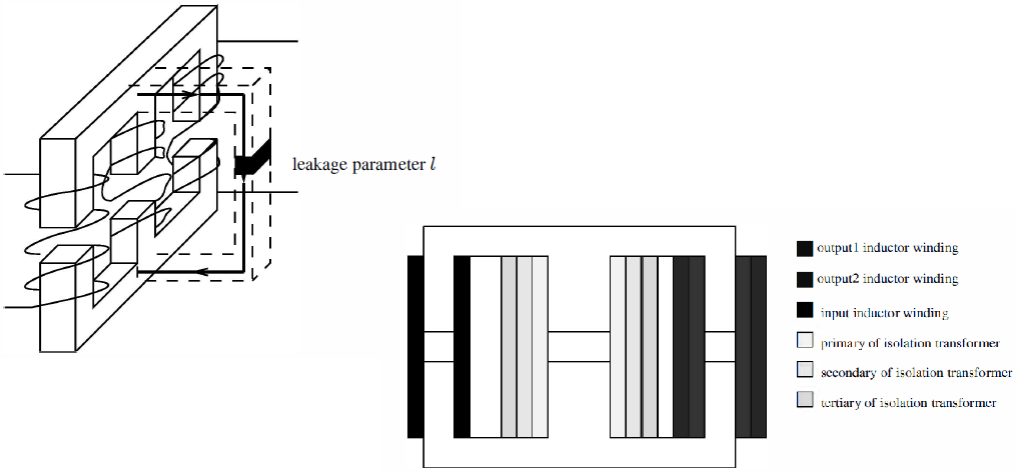

Figure 3.3: Core Structure and Leakage Parameter Characterization

reluctance of the center flux path, which is approximately constant for a type of core or the air-gap. This parameter is vital to the design process and used much in the later design stages.

We also note that the leakage inductance of the isolation transformer referred to the primary can be effectively described by the following equation :

$$l = \mu_0 S R_l \tag{3.1}$$

$$L_l \approx L_{l_1} + \frac{L_{l_2}}{{n_1}^2} \parallel \frac{L_{l_3}}{{n_2}^2} \tag{3.2}$$

where the parameters on the RHS are illustrated in Fig.3.2.

The isolation transformer can now be effectively considered as a single winding, with a large magnetizing inductance M and a leakage inductance L_l.

3.3.3 Magnetic Circuit Analysis

The effective three-winding structure, derived in Section B can be represented by Fig. 3.4(a). The (effective) single winding on the center leg has N turns and all the input and output windings have same number of turns (N1), when referred to the primary. The corresponding flux-reluctance circuit is shown in Fig. 3.4(b), and using duality-transformation, the inductance (dual) model is obtained [26], which is shown in Fig.

Table 3.1: Magnetic Circuit

Parameter	Description
l	leakage parameter
B_m	saturation flux density
L	center leg inductance
S	center-leg cross-section
N	no. of turns of transformer primary
N_1	no. of turns of input inductor winding
I_1	input inductor dc current
I_2	output inductor dc current
I	center leg peak current
$x/2$	spacer air gap

3.4(c). The parameters of Fig. 3.4 and others used in design are described in Table 3.1. It is worth noting that

$$I_2 = n_1 I_{grid} + n_2 I_{battery} \tag{3.3}$$

where I_{grid} and $I_{battery}$ are the dc currents being drawn by the grid and storage port respectively at nominal load when the PV module is in operation.

The reluctances and inductances are defined by the following equations :

$$R = \frac{x}{\mu_0 S/2}, \quad L_m = \frac{N^2}{R} \tag{3.4}$$

Ac (zero-ripple) analysis

Fig. 3.5(a) basically describes the ripple circuit for the reluctance model. Since all the ripple is shifted to the center winding, the mmf sources are shorted on the outer legs. The resulting circuit is then solved to get the following condition:

$$\frac{R}{R_l} = \frac{N_1}{N} - 2 \tag{3.5}$$

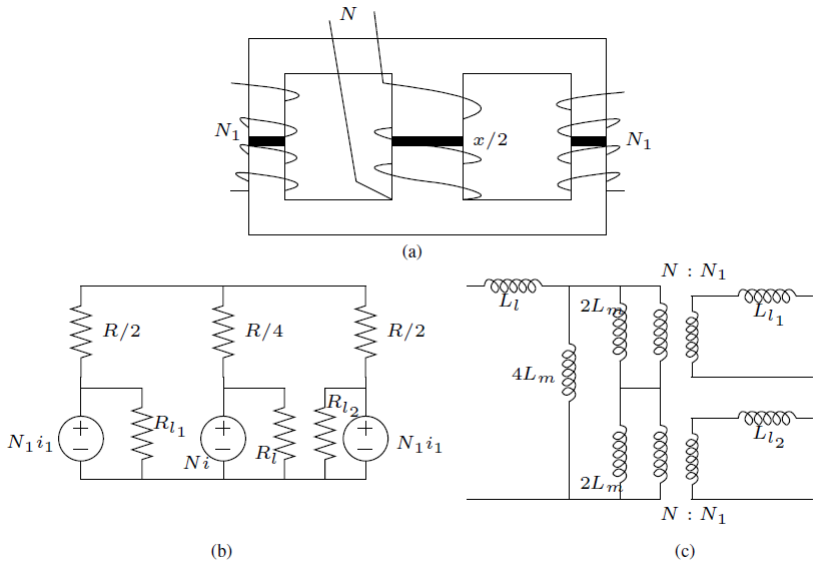

Figure 3.4: (a) Effective three-winding structure, (b) Corresponding magnetic circuit, (c) Corresponding inductance (dual) model.

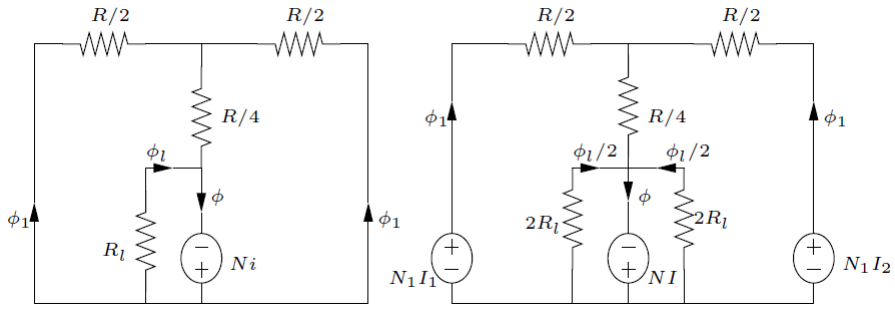

Figure 3.5: (a) ac reluctance model, (b) dc reluctance model.

This implies

$$\frac{x}{l} = \frac{N_1}{2N} - 1 \tag{3.6}$$

Dc analysis: Fig. 3.5(b) describes the magnetic circuit at the dc operating point. This figure is derived from Fig. 3.4(b) after neglecting L_{l_1} and L_{l_2}, as explained earlier in Section 3.3.2. To prevent core saturation, we have the following design equation(worst

case) for S [26]:

$$\frac{B_m S}{2} \geq \frac{NI + N_1(1.5I_1 - 0.5I_2)}{R} + \frac{NI}{2R_l}, I_1 > I_2 \tag{3.7}$$

which is obtained by solving the circuit in Fig. 3.5(b) for ϕ and considering flux saturation in the center leg. (It can be seen that the center leg will carry the maximum amount of flux, hence will saturate earlier than the other two legs)

Center Leg Inductance Requirement

We impose an additional requirement that decides the amount of ripple allowed on the center winding. With this chosen to be approximately 150% of the DC current through the center winding (or equivalently the magnetizing inductance M in Fig. 3.1), and

$$L = \mu_0 S N^2 (\frac{1}{x} + \frac{1}{l}) \tag{3.8}$$

where L is the inductance looking into the winding on the center leg (Fig. 3.4(a)) with the other windings shorted, we have another design equation for the problem.

Additionally,

$$L_l = \frac{\mu_0 S N^2}{l} \tag{3.9}$$

Equations (3.6),(3.7),(3.8),(3.9) give us a set of design equations for choosing the air-gap x and cross-sectional area S, once it is known what l is, i.e., after the core is wound in a particular way(eg. Fig. 3.3). However, one needs to chose N carefully. Too large a value of N will make the design large, while a very small value might make the design very inefficient[10].

Assuming a value of l = 2mm and saturation flux density of B_m = 1.5T (Metglas 2605SA1 datasheet), the critical number of turns of the transformer primary is calculated(which causes blow-up of the spacer gap length) as $N_{c0} = \frac{B_m l}{\mu_0 I_e}$. This gives an initial guess for $N : N_0 = 0.2 N_{c0}$ and subsequently for $S_0 = \frac{L I_e}{B_m N_0}$ is made[26]. This L_l is the same as (1), provided the assumptions in 3.3.2 are valid. The value of L comes from the ripple requirement on the center winding, prior to the actual design. We select the closest cross-section available from a standard core manufacturer's list, and the corresponding value of l. The solution of the equations (3.6)-(3.9) in the respective order followed by transformer scaling gives the desirables.

3.4 Power Modes and Simulation Results

Specifications for the converter are chosen keeping in mind a typical PV microgrid, and plug-in hybrid charging voltages (at the storage port). An issue to be noted here is that the maximum power P_o is limited by the saturation flux density B_m. This is because once we fix the voltages (eg. for typical PV-microgrid converters), the power becomes fixed on account of the maximum dc current being limited by B_m. This can be proved by analyzing the equations (3.5)-(3.8), as was done in [26]. Having $B_m = 1.5$T allows us to go upto $P_o = 250$W. Due to this kind of power rating, it is ideal to use this as a module in a larger power system. The proposed converter was simulated with the specifications listed in Table II and the design parameters (using an EE-16 core) enlisted in Table III. These parameters have been described earlier in figures 3.1, 3,2 and 3.4.

The following modes of operation are explored in this paper:

- **Mode 1**: The PV source supplies power to the grid and charges the battery.
- **Mode 2**: The PV source is offline. The battery is charged from the grid.
- **Mode 3**: The PV source is offline. The battery supplies power to the grid.

The simulation results for these modes are shown in Figures 7, 8 and 9 respectively.

The ripple is approximately 1-2% in **Mode 1**, for which the nominal design has been done. The other modes have approximately 4-5% ripple, operating with the PV port offline, which presents a respectable performance.

Apart from this, the voltage excursion at the output terminals is also fairly decent and does the require the use of bulky capacitors, as can be seen in Figures 10-12. In fact, the use of a capacitor causes some undesired spikes in the current waveforms, as mentioned in [26]. Hence, if at all, we require some ripple power to be supplied, as in the case of the dc-bus tied to the grid, the capacitor is to be added in the inverter stage.

Finally, finite element methods are employed for the effective three-winding structure to generate the flux density patterns. A custom core closely resembling the shape and size of an EE-13 core is built using ANSYS Maxwell® and simulated using the magnetostatic solver. An efficiency of 95% is noted.

Table 3.2: Specifications

P_o	$250W$
V_{in}	$30V$
V_{grid}	$400V$
$V_{battery}$	$240V$
n_1	13
n_2	8
$\bar{D}$	0.5

Table 3.3: Design values

$l = 1.33\text{mm}$	$B_m = 1.5\text{T}$
$S = 0.16\text{cm}^2$	$N_1 = 48$
$N = 19$	$x = 0.27\text{mm}$
$C_a = 47\mu F$	$C_b = 0.5\mu F$
$C_c = 1\mu F$	$R_{battery} = 460.8\Omega$
$R_{grid} = 1216\Omega$	$I_1 = 8.55A$
$I_2 = 8.5A$	$I = 25.6A$

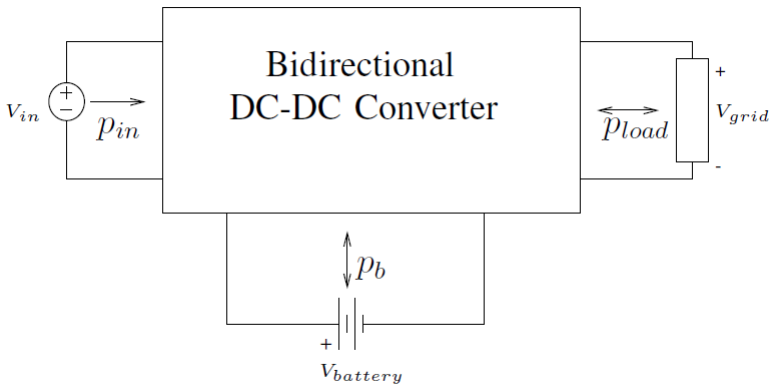

Figure 3.6: Power Modes explored for the Ćuk Converter

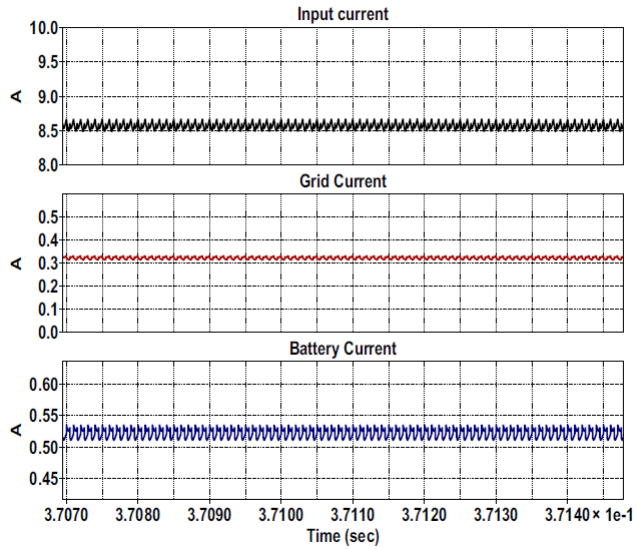

Figure 3.7: Terminal currents for Mode 1

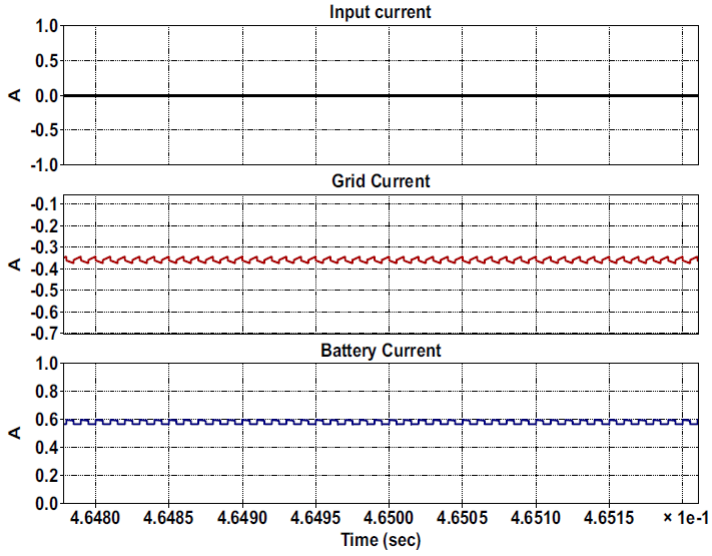

Figure 3.8: Terminal currents for Mode 2

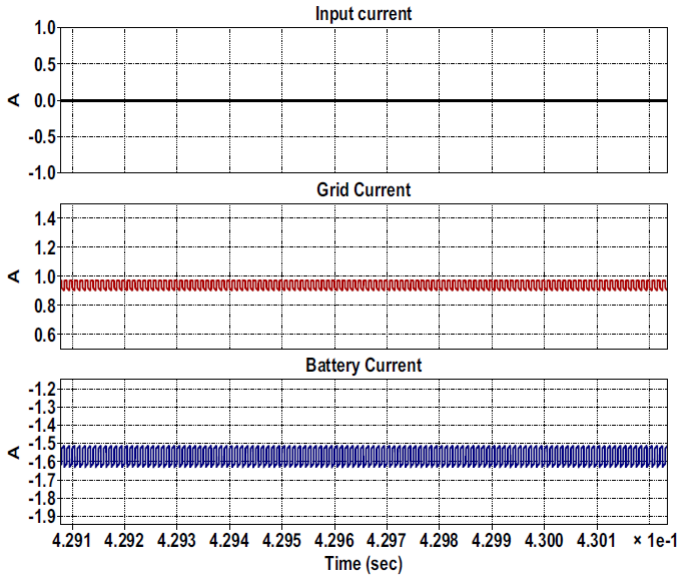

Figure 3.9: Terminal currents for Mode 3

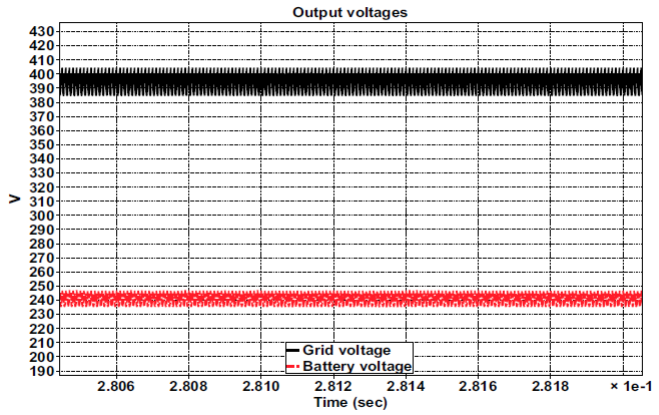

Figure 3.10: **Mode 1**: output voltage waveforms

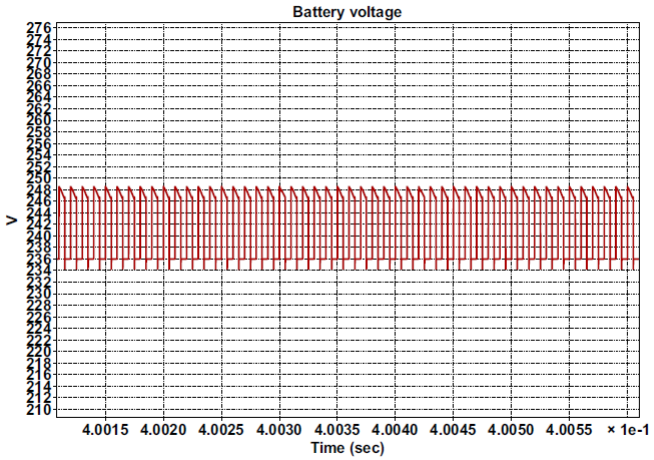

Figure 3.11: **Mode 2**: output voltage waveforms

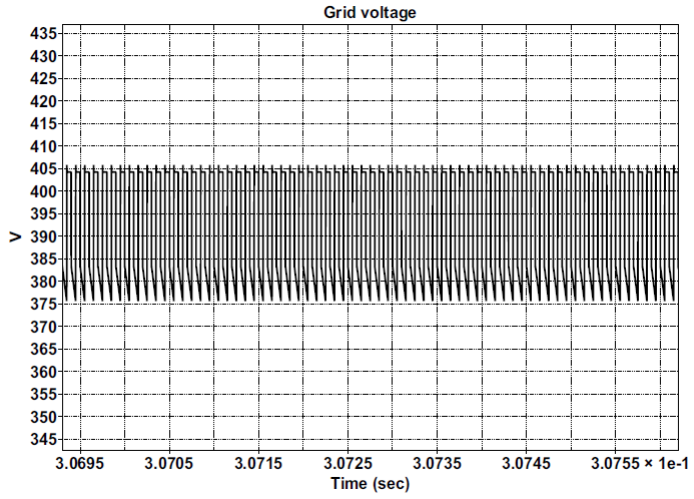

Figure 3.12: **Mode 3**: output voltage waveforms

3.5 Finite-Element Modelling of the EE-core

This is a hugely important step in going towards the hardware and gives us a first hand idea of what to expect while designing for the zero-ripple condition. The purposes of the FEM analysis is include the following :

- To validate the leakage parameter assumption.
- To validate the flux simulations.
- To optimize the core and winding dimensions for efficiency.

In this thesis, only the first two have been demonstrated. A core is chosen with the following dimensions :

$a = 4mm, h_a = 25mm, d = 4mm$, so that it is commensurate with the simulation design. The core material is Ferrite.

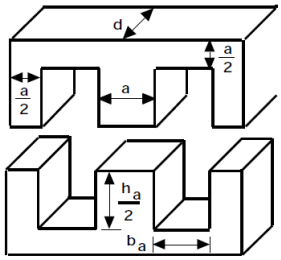

Figure 3.13: Core Dimensions

Corresponding to the positive, negative peaks of the center winding current as well the zero point of the current (refer Fig.3.14), we have the flux plots as shown below, with air-gap g=2.5mm. (Fig. 3.16)

Then an air-gap sweep is done with the above core dimensions. The results are shown in spreadsheet format (Fig.3.15). L_{11} is the extracted self-inductance of the center winding. Using the circuit given in Fig.3.4(c), The magnetizing inductance L_m can be calculated, followed by the leakage parameter l.

The plots in Fig. 3.16 show that the model of the three winding structure with the leakage parameter l converges to the actual model near the zero-ripple condition, which is intuitively correct. The onus is to desensitize the design such the experimental N_1/N curve is very close to the N_1/N (actual). Hence this confirms the validity of the leakage

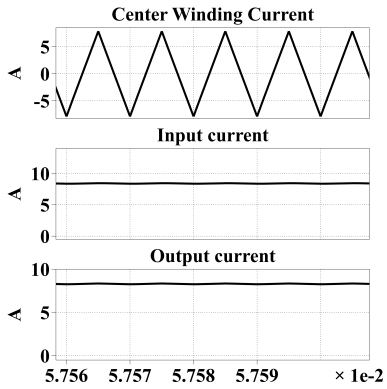

Figure 3.14: Current waveforms in the windings

g	2d measured/m(mH)	L11	R	Lm	actual l	N1/N(calc)	N1/N(actual)	Diff^2	l(from zero-ripple condition)
1.00E-03	1.64	6.56E-06	2.12E+08	1.70E-06	2.30E-03	2.87E+00	2.526315789	0.118802893	0.0038
1.50E-03	1.2933	5.17E-06	2.48E+08	1.45E-06	3.20E-03	2.94E+00	2.526315789	0.167952306	0.0057
2.00E-03	1.1053	4.42E-06	2.65E+08	1.36E-06	4.27E-03	2.94E+00	2.526315789	0.169251153	0.0076
2.50E-03	0.99261	3.97E-06	2.72E+08	1.33E-06	5.50E-03	2.91E+00	2.526315789	0.145951741	0.0095
3.00E-03	0.89735	3.59E-06	2.73E+08	1.32E-06	7.68E-03	2.78E+00	2.526315789	0.064931024	0.0114
3.50E-03	0.8311	3.32E-06	2.70E+08	1.34E-06	1.11E-02	2.63E+00	2.526315789	0.010663602	0.0133
4.00E-03	0.77075	3.08E-06	2.65E+08	1.36E-06	2.00E-02	2.40E+00	2.526315789	0.016019483	0.0152
4.50E-03	0.72322	2.89E-06	2.59E+08	1.39E-06	6.63E-02	2.14E+00	2.526315789	0.152556016	0.0171
5.00E-03	0.68366	2.73E-06	2.53E+08	1.43E-06	-5.95E-02	1.83E+00	2.526315789	0.482079352	0.019
5.50E-03	0.64916	2.60E-06	2.46E+08	1.47E-06	-2.13E-02	1.48E+00	2.526315789	1.086263451	0.0209
6.00E-03	0.61862	2.47E-06	2.39E+08	1.51E-06	-1.32E-02	1.09E+00	2.526315789	2.054215159	0.0228
3.70E-03	0.80336	3.21E-06	2.68E+08	1.34E-06	1.38E-02	2.53E+00	2.526315789	4.46868618	0.01406

Figure 3.15: Comparison of analytical and FEM results for the leakage parameter l

parameter assumption. Hence an area of future research is that apart from optimizing the core design for losses, it also needs to be optimized for desensitivity, like adding more winding area to the center windings. Formulation of the core in this regard needs to be done.

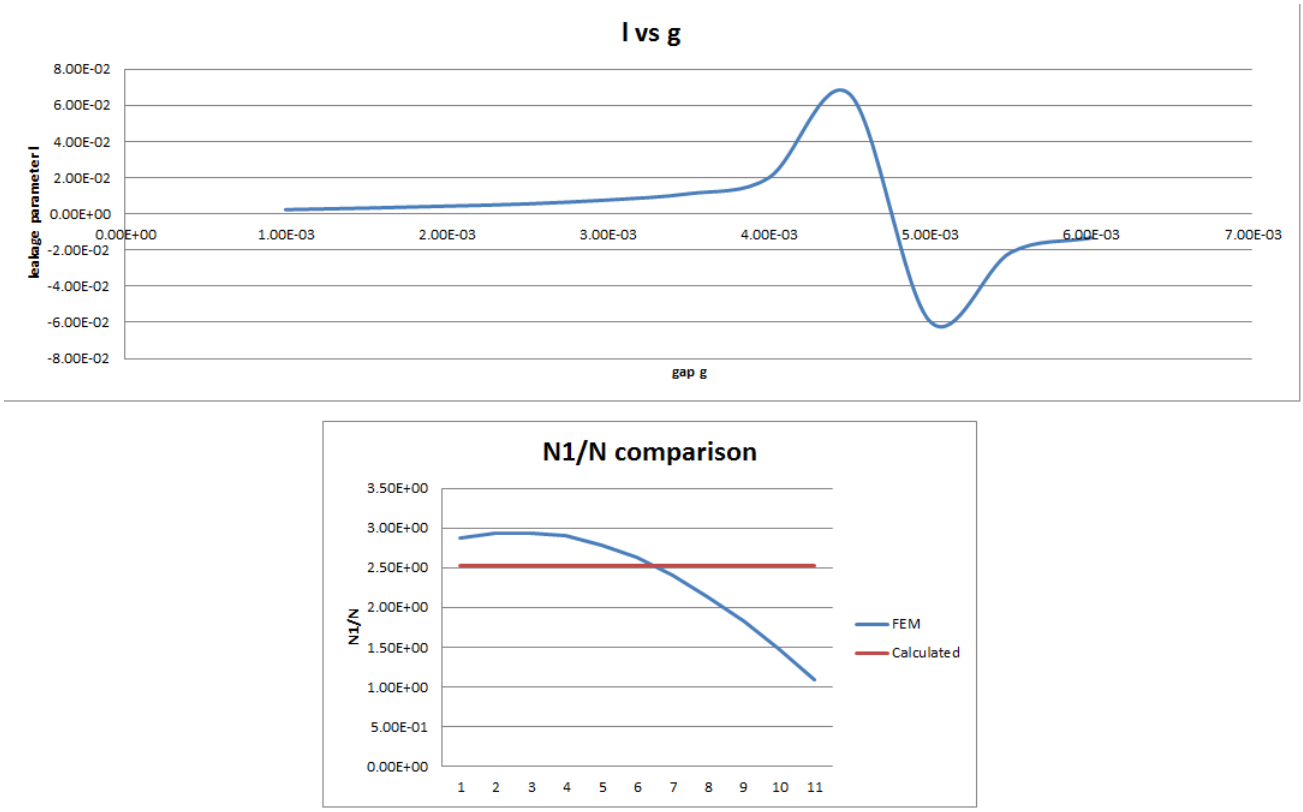

Figure 3.16: Comparison Plots

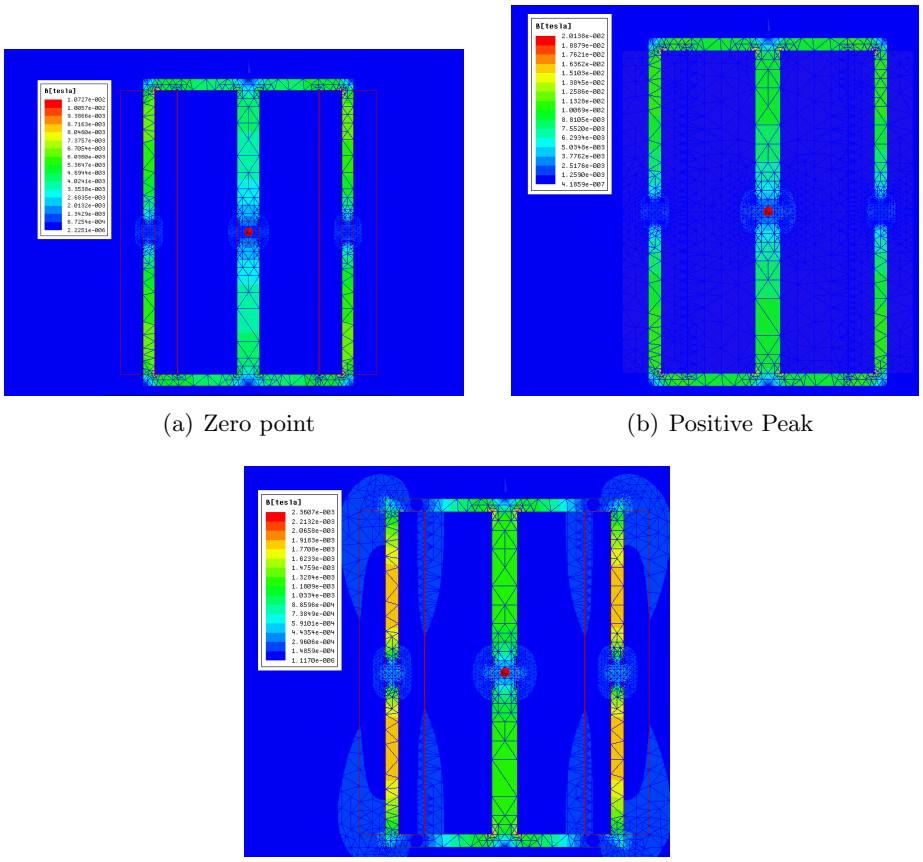

(a) Zero point

(b) Positive Peak

(c) Negative Peak

Figure 3.17: Flux plots for the important points in the center winding current waveform

Chapter 4

Soft-Switching Scheme in Two-port Converter with Integrated Magnetics

4.1 Topology Choice for Photovoltaics

Historically, the boost converter is the simplest solution for PV application since it has a low part count and a simple design [19]. However, these converters suffer from high conduction losses and result in low efficiency power conversion due to requirement of very large duty ratio ($D > 90\%$ to convert a single cell voltage of 2.3V to 24.6V). Furthermore, input current ripple plays a key role in the performance of these converters which results in requiring a large input inductor [19].

The full bridge converter is one of the most commonly employed isolated topologies for photovoltaic applications [20]. This power converter is composed of four switches, an isolation transformer and an output rectifier. The added power stages and components leads to reduced reliability, lower power density and higher cost.

Resonant converters have also been considered for building high power density converters [21]. These converters can operate at high switching frequencies with natural zero-voltage switching [21]. However, they suffer from complex design, low controllability and reduced efficiency at partial loads.

The Ćuk Converter

The Ćuk converter is optimal for PV conversion primarily because of its wide dynamic range. It is also able to effectively operate as a dc transformer because of clean input and output currents via means of integrated magnetics [22]. Other improvements on the basic Ćuk converter include the active-clamp technique proposed in [23]. This non-isolated Ćuk converter achieves ZVS turn-on of all the active switches. The isolated topology proposed in [24] also achieves ZVS turn-on but uses a second transformer and diode on the input side in addition to the additional components suggested in [23]. The method proposed in [25] for the isolated converter utlises the leakage inductance of the isolation transformer and the clamp capacitor to achieve resonance. However, the clamp capacitor is in principle supposed to be a fixed voltage source. Also, none of these topologies utilise the integrated magnetics extension of the Ćuk converter.

This thesis builds upon the cited prior work and addresses all the demands of a typical PV-to-grid converter. It presents the analysis, design and simulation of an isolated Ćuk converter (Fig.4.1) which uses a combination of active and passive soft-switching methods to achieve high efficiency, which is of paramount importance in a PV-to-grid interface. The active-clamp technique is utilised with C_r and L_r to achieve ZVS turn-on of the switches S_1 and S_2. The passive snubber elements L_{r2} and C_{r2} superimpose a high-frequency(several orders higher than switching frequency f_s) ripple current on top of the switch currents and provide a freewheeling path such that ZCS turn-off of the switches is also achieved. In addition to this, the input and output inductors L_1 and L_2 along with the isolation transformer are integrated into a single magnetic core and the corresponding magnetic circuit is analysed to achieve nearly-zero ripple on the input and output currents. This will reduce the demands on the controller as there will be negligible excursion from the maximum power-point of the PV module. Finally, these devices have reduced voltage and current stresses on the main switch and allow operation at high frequency.

This chapter is organized as follows. The design of the integrated magnetics is explained in Section 4.2. The steady-state analysis of the active-clamp converter is presented in Section 4.3. Section 4.4 deals with the design issues and simulation results. Conclusions and Future Work are presented in Section 4.5.

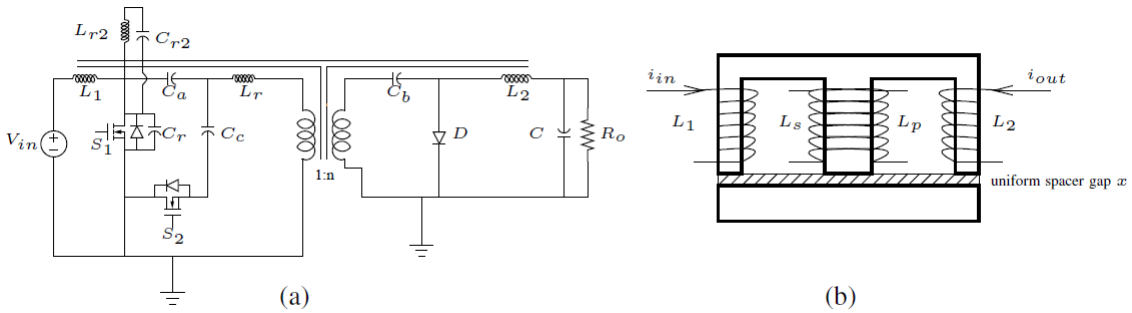

Figure 4.1: ZVS-ZCS Active-Clamp Ćuk Converter with Integrated Magnetics

4.2 Magnetics Design

Nomenclature

l	leakage parameter
B_m	saturation flux density
L	center leg inductance
S	center-leg cross-section
N	no. of turns of transformer primary
N_1	no. of turns of input inductor winding
N_1	no. of turns of reflected output inductor winding
I_1	input inductor dc current
I_2	output inductor dc current
I	center leg peak current
x	spacer air gap
μ_0	permeability of free space

The design of the magnetic circuit for zero ripple at input and output ports essentially depends on appropriately assigning the air-gap, with respect to the amount of leakage flux on the center winding of the core shown in Fig.4.1. The leakage on the outer limbs is assumed to be negligible compared to the center winding, so as to aid in the magnetics design. As explained in [26], the design of the integrated magnetics is greatly facilitated by the introduction of a leakage parameter which is constant for a given type of core. It is calculated from $l = \frac{\mu_0 S N^2}{L_l}$.

Assuming a value of $l = 2mm$ and saturation flux density of $B_m = 1.5$T (Metglas

core), the critical number of turns of the transformer primary is calculated(which causes blow-up of the spacer gap length) as $N_{c0} = \frac{B_m l}{\mu_0 I_e}$. This gives an initial guess for N : $N_0 = 0.2N_{c0}$ and subsequently for $S_0 = \frac{LI_e}{B_m N_0}$ is made [23]. The value of L comes from the ripple requirement on the center winding, prior to the actual design. We select the closest cross-section available from a standard core manufacturer's list. The solution of the following equations [**?**] is then solved in the respective order. This generates a kind of zero-ripple design for a three-winding non-isolated Ćuk converter [22]. This step is followed by a simple transformer scaling on the center winding to give the desirables :

$$N = \frac{LI_e}{B_m S} \quad \text{dc saturation}(I_e = I + 3I_1 - I_2) \tag{4.1}$$

$$L_l = \frac{\mu_0 N^2 S}{l} \quad \text{leakage inductance} \tag{4.2}$$

$$N_1 = 2N\frac{L}{L - L_l} \quad \text{zero-ripple condition} \tag{4.3}$$

$$x = \frac{1}{2} \cdot \frac{L_l}{L - L_l} \cdot l \quad \text{definition of } L \tag{4.4}$$

4.3 Soft-Switching Mechanism

To simplify the analysis, the input and output currents are assumed to be pure dc (the integrated magnetic structure aids in this approximation and removes the need for bulky inductors as in [23]). The energy transfer capacitors C_a, C_b, the clamp capacitor C_c are also fairly large compared to the snubber capacitors C_r and C_{r2}, hence they can be assumed as fixed voltage sources.

The six main stages of the active-clamp converter are shown in Fig.4.2 and the expected theoretical waveforms are shown in Fig.4.3. The switching cycle starts at $t = 0$, when switch S_1 is turned off(Fig.4.2(a)). The capacitor is now charged under nearly a constant current $\sim I_{in} + nI_o$. The current is slightly off this value due to a small high-frequency($>> f_s$)oscillating current in the snubber branch (L_{r2}, C_{r2}), which helps to achieve the ZCS turn-off of S_1 as it delays the build-up of the voltage across S_1 while the current through the switch goes to zero(refer Fig.4.4). At $t = t_0$, we have :

$$\frac{dv_{C_r}}{dt} = \frac{I_{in} + nI_o}{C_r + C_{r2}} + \frac{C_{r2}L_{r2}}{C_r}\frac{d^2 i_{L_{r2}}}{dt^2} \tag{4.5}$$

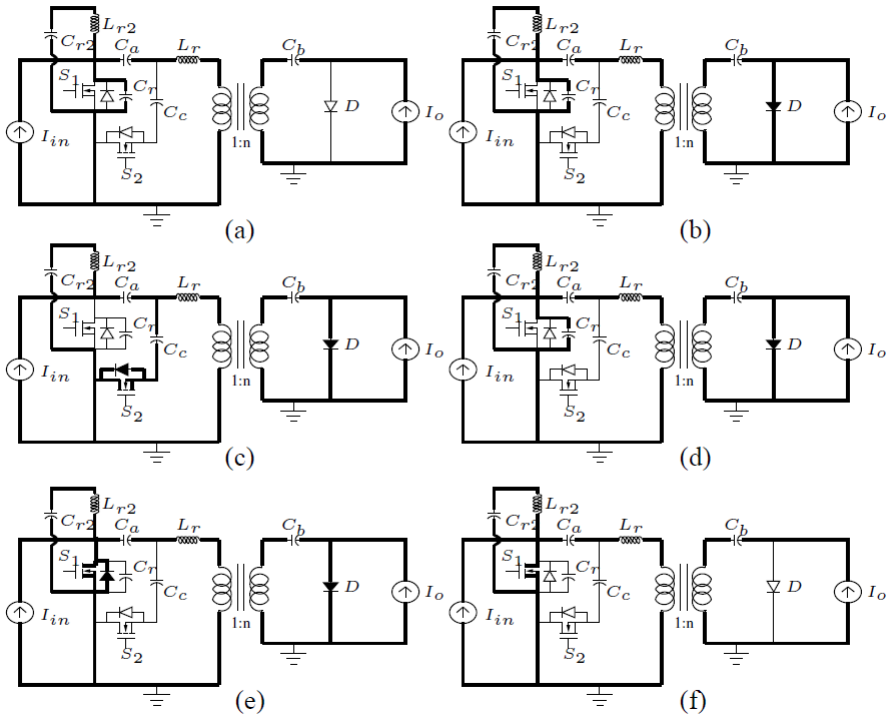

Figure 4.2: ZVS-ZCS Intervals

Since we are looking at the frequency regime f_s=100 kHz, we can represent the second term in the equation by its average value over the time period decided by the resonant frequency $f_{r2} = \frac{1}{2\pi\sqrt{L_{r2}C_{r2}}}$ which is several orders of magnitude higher than f_s(by design). Since $\frac{d^2 i_{L_{r2}}}{dt^2}$ is a sinusoid, its average is zero. Hence without the presence of this snubber branch(L_{r2}, C_{r2}), ZCS turn-off of S_1 would be much more difficult to achieve. The novelty of this scheme lies in the fact that C_{r2} allows an additional degree of freedom to achieve the ZCS turn-off. At other times, its effect is negligible.

Coming back to the main soft-switching regime, this charging operation of C_r continues until $v_{C_r} = V_{in} + \frac{V_o}{n}$. This happens at $t = t_1$, when D turns on(Fig.4.2(b)). In the next interval, L_r and C_r undergo resonance until $v_{C_r} = V_{in} + V_{C_c}$ at $t = t_2$, when the antiparallel diode of S_2 becomes forward-biased(Fig.4.2(c)). At this moment, S_2 can be turned on at zero-voltage. Thus begins the second quasi-steady state of the

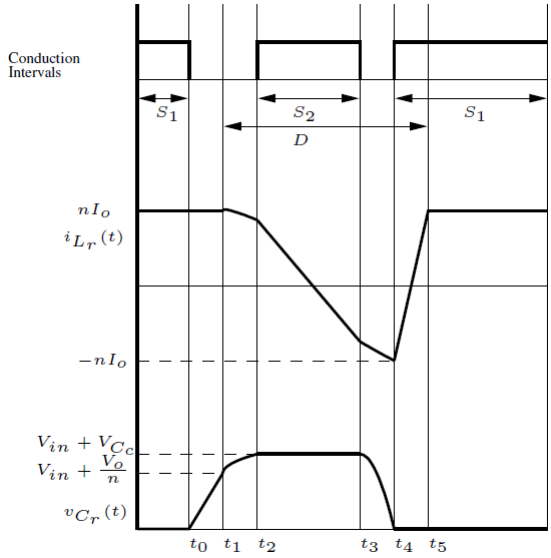

Figure 4.3: Theoretical Waveforms of the proposed Ćuk Converter

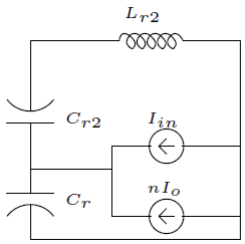

Figure 4.4: Circuit at $t = t_0$

converter(Fig.4.2(d)). During this time, the current through L_r ramps down. It terminates at $t = t_3$, when we turn off S_2. This also occurs with ZCS using the same mechanism with the passive snubber elements L_{r2} and C_{r2} described earlier. Now the voltage across C_r drops until it reaches zero at $t = t_4$. S_1 can be turned on at this time at zero-voltage(Fig.4.2(e)). The current through L_r will now ramp up until it reaches nI_o, turning D off at $t = t_5$(Fig.4.2(f)). This returns the circuit to the state same as the beginning.

4.4 Design Considerations and Simulation Results

In order to make the topology work in the way described in Section III, there are several design constraints:

1. $V_{C_c} > \frac{V_o}{n}$ for the forward diode D to turn on before the antiparallel diode of S_2. A transformer between the output voltage and the clamp capacitor with a turns ratio $1 : n_2$, where $n_2 < n$ will allow this.

2. Since the voltage across C_c is fixed, $\int_0^{T_s} i_{C_c}\,\mathrm{d}t = 0$. This gives $V_{C_c} \sim \frac{2nI_oL_r}{(1-\bar{D})T_s}$.($\bar{D}$ = duty ratio, T_s = time period)

3. For $t_2 > t_1$ in Fig.3,i.e., for quasi-resonance to occur in the desired way, we must have $L_rC_r \leq \frac{1}{4{f_s}^2}$. This along with points (2) and (1) give us design equations for L_r and C_r.

4. From (5), C_{r2} should be roughly or near about of the order of C_r. Too large a value of C_{r2} will increase the amplitude of the oscillating current substantially, while a very small value will have no effect at all. For this simulation, we have chosen $C_{r2} \sim 2C_r$. The value of C_{r2} can in fact be chosen using the MOSFET specifications. From the switching frequency requirement, $L_{r2}C_{r2} << \frac{1}{4\pi^2{f_s}^2}$.

The proposed converter was simulated with the following specifications : $P_o = 180W$,$V_{in} = 30V$,$V_{out} = 250V$, $n = 10$ and $\bar{D} = 0.48$ (allowing room for a bit of overdesign). The parameters of the designed circuit were(using an EE-13 core) :

$l = 1.33$mm	$B_m = 1.5$T
$S = 0.16\text{cm}^2$	$N_1 = 48$
$N = 19$	$x = 0.27$mm
$C_a = 5\mu F$	$C_c = 100\mu F$
$C_r = 1nF$	$C_{r2} = 2nF$
$L_{r2} = 1\mu H$	$L_r = 0.625\mu H$
$C_b = 4.2\mu F$	$R = 360\Omega$
$C = 0.21\mu F$	

Fig. 4.6 shows that very low ripple is achieved in the input current(around 5%) while zero-ripple is achieved on the output current. The slight ripple in the input current is

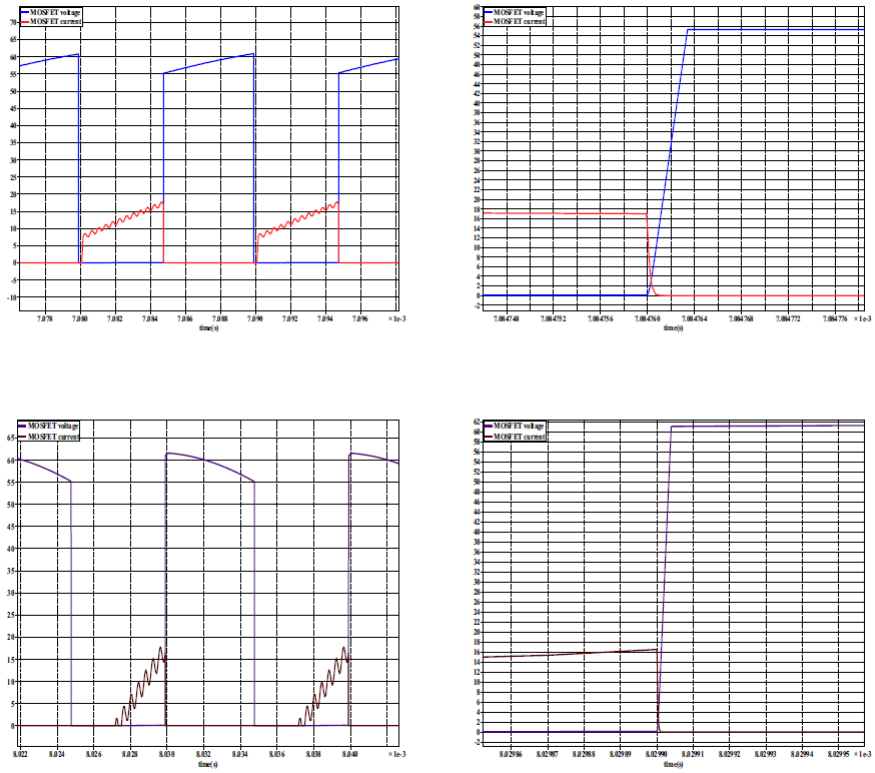

Figure 4.5: (a) ZVS turn-on of S_1 (b) zoomed plot showing ZCS turn-off of S_1 (c) ZVS turn-off of S_2 (d) zoomed plot showing ZCS turn-off of S_2

due to the presence of the ZVS-ZCS components on the input side of the isolation transformer and subsequent loss of symmetry. Fig. 4.7 shows the resonant inductor L_r current and capacitor C_r voltage waveforms. Fig. 4.5 shows that the ZVS-ZCS objectives are achieved for MOSFETS S_1 and S_2.

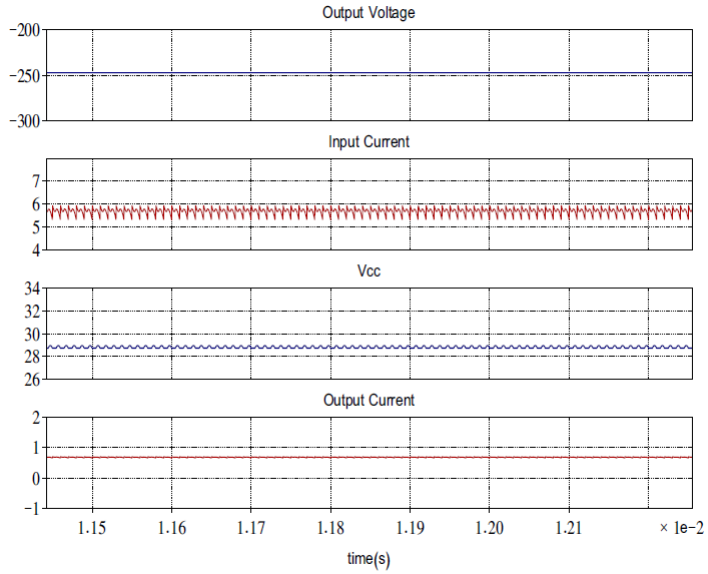

Figure 4.6: Input and Output currents, output voltage and clamp capacitor voltage

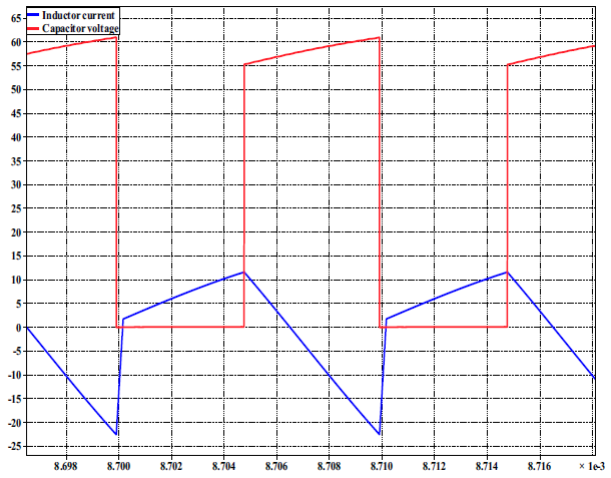

Figure 4.7: Current in L_r and Voltage in C_r

Chapter 5

Conclusion and Future Work

Multi-port Converters are becoming extremely popular in recent literature for their applications in renewable energy power distribution. This can be attributed to their plug and play capability, and being able to interface widely nominal voltages. However the onus is to reduce the part count and integrate the components as much as possible, without sacrificing the power quality, reliability or efficiency.This thesis addresses this need by arguing the case for variants of the Ćuk Converter as a promising topology in this regard. Both the topologies have the advantage of an integrated magnetic structure, which reduces part count, improves efficiency and have enhanced performance in terms of emulating a perfect DC-DC transformer, which is the principal goal of a switched-mode converter. A three-port converter has been proposed in this thesis which has the ability to integrate renewables, storage and the grid through a common power path. The thesis also demonstrates the addition of a novel soft-switching scheme, which increase efficiency and reduce component stress, in addition to the integrated magnetics enhancement.

5.1 Conclusion

Chapter 2 introduces the concept of magnetic integration and discusses the advantages of having such a structure. The basic idea for this integration lies behind the fact that windings with proportional voltage waveforms can be coupled onto a single magnetic structure. This is actually the reversal of the cause-and-effect in a two-winding transformer. The idea can obviously be extended to three windings. This idea is demonstrated in the basic Ćuk topology. The magnetic scaling law quantitatively demonstrates

the advantages to be gained in power density of such a structure. We also delve deeper to find that an improvement in performance can also be obtained in terms of zero-ripple terminal currents, apart from the gain in power density. However, although the circuit equations (inductance matrix model) can be solved to yield a condition, it does not say much about the actual design. Also, it is discussed why the brute-force approach of using the inductance matrix is ill-conditioned for numerical computations.

With the conclusions of Chapter 2, Chapter 3 explains a more structural design approach for a Three-port Bidirectional Ćuk Converter while still adhering to the circuit equations. The EE-core is chosen for symmetry reasons, while still maintaining the simplicity of a 2-dimensional core. The first thing is to realize that a six-winding structure is a nightmare to analyze in terms of equations, so there must be a trick to scale it to a smaller problem. Once this is shown, the next thing is identify the main leakage paths. A crucial design step is to have more leakage in the center (transformer) winding. With this assumption, a physical magnetic circuit of the core can be derived. From this, a circuit version can be obtained using the duality principle of circuit theory. This is a inductance only circuit, and interwinding capacitances and DC resistances have been left for finite element modelling. The circuit can be used to obtain the zero-ripple condition. Although this phenomenon only deals with the ac model of the flux-reluctance circuit, the dc model is actually needed for the complete design because of flux saturation. A further design equation comes from the center leg ripple requirement. All these can be solved in the proper order to design the core. The rest of the converter is standard SMPS (switched-mode power supply) design. After this converter is designed, simulations are done to investigate the various possible modes of operation of the converter.

Even with this performance improvement, it remains to be seen whether further efficiency improvements can be added, especially by soft-switching. In Chapter 4 such a scheme is explained. Some new components are added, an extra switch and clamp capacitor to achieve ZVS turn-on of the switches. Also a high-frequency resonant snubber branch is added for achieving close to ZCS turn-off of the switches. All these reduce switch voltage stresses. However, there is also an inherent loss of symmetry in the converter structure once the components are added. This affects the "proportional voltage waveform" requirement for the zero-ripple while adding efficiency enhancement. This tradeoff is the investigation of the simulation in this chapter.

5.2 Future Work

There is a plethora of future research incentives for such a topology. These are :

- Carrying out the FEM to extract leakage inductances and more importantly, a way to calculate the leakage parameter l from the same solution.
- Hardware results to validate the zero-ripple after appropriate trade-offs in core and copper losses have been analyzed as per efficiency (90-95%) requirements. The effect of interwinding capacitances are also important.
- Addition of soft-switching to the three-port converter.
- A unified design for three modes of operation, irrespective of whether one port is online/offline.
- An elegant small signal-model of such a converter, which does justice to the magnetic circuit counterpart.
- A multiport robust controller design in order to have effective power management schemes for the three ports.
- Investigation into a four-port extension of such a converter. Probably requires a unique magnetic structure and the extra-port can be incorporated into the circuit by means of Middlebrook's extra-element theorem.

Chapter 6

References

[1] US Department of Energy. http://www.eia.doe.gov.

[2] Energy Information Administration. Annual energy outlook 2011. http://www.eia.doe.gov.

[3] Tax credit in doubt, wind power industry is withering. http://www.nytimes.com/2012/09/21/business/energy-environment/as-a-tax-credit-wanes-jobs-vanish-in-wind-power-industry.html?pagewanted=all&_r=0.

[4] Glut of solar panels poses a new threat to china. http://www.nytimes.com/2012/10/05/business/global/glut-of-solar-panels-is-a-new-test-for-china.html?pagewanted=all.

[5] Renewable portfolio standards. http://www.epa.gov/chp/state-policy/renewable_fs.html.

[6] Arctic ice melting at 'amazing' speed, scientists find. http://www.bbc.co.uk/news/world-europe-19508906.

[7] Plug-in cars could actually increase air pollution. http://usatoday30.usatoday.com/tech/products/environment/2008-02-25-plug-in-hybrids-pollution_N.htm.

[8] Electropaedia. http://www.mpoweruk.com/solar_power.htm.

[9] Dakota county utility gets special electric car rate approved. `http://www.startribune.com/business/174817091.html?refer=y`.

[10] US Department of Energy. Fuel cell vehicles. `http://www.startribune.com/business/174817091.html?refer=y`.

[11] Chuanhong Zhao and J.W. Kolar. A novel three-phase three-port ups employing a single high-frequency isolation transformer. In *Power Electronics Specialists Conference, 2004. PESC 04. 2004 IEEE 35th Annual*, volume 6, pages 4135–4141 Vol.6, June 2004.

[12] Yen-Mo Chen, A.Q. Huang, and Xunwei Yu. A high step-up three-port dc-dc converter for stand-alone pv/battery power systems. *Power Electronics, IEEE Transactions on*, 28(11):5049–5062, Nov 2013.

[13] Zhan Wang and Hui Li. An integrated three-port bidirectional dc-dc converter for pv application on a dc distribution system. *Power Electronics, IEEE Transactions on*, 28(10):4612–4624, Oct 2013.

[14] S. Falcones, R. Ayyanar, and Xiaolin Mao. A dc-dc multiport-converter-based solid-state transformer integrating distributed generation and storage. *Power Electronics, IEEE Transactions on*, 28(5):2192–2203, May 2013.

[15] Hongfei Wu, Kai Sun, Runruo Chen, Haibing Hu, and Yan Xing. Full-bridge three-port converters with wide input voltage range for renewable power systems. *Power Electronics, IEEE Transactions on*, 27(9):3965–3974, Sept 2012.

[16] F. Nejabatkhah, S. Danyali, S.H. Hosseini, M. Sabahi, and S.M. Niapour. Modeling and control of a new three-input dc-dc boost converter for hybrid pv/fc/battery power system. *Power Electronics, IEEE Transactions on*, 27(5):2309–2324, May 2012.

[17] Hongfei Wu, Runruo Chen, Junjun Zhang, Yan Xing, Haibing Hu, and Hongjuan Ge. A family of three-port half-bridge converters for a stand-alone renewable power system. *Power Electronics, IEEE Transactions on*, 26(9):2697–2706, Sept 2011.

[18] Hariharan Krishnaswami and N. Mohan. Three-port series-resonant dc-dc converter to interface renewable energy sources with bidirectional load and energy storage ports. *Power Electronics, IEEE Transactions on*, 24(10):2289–2297, Oct 2009.

[19] M.S. Agamy, M. Harfman-Todorovic, A. Elasser, J.A. Sabate, R.L. Steigerwald, Yan Jiang, and S. Essakiappan. Dc-dc converter topology assessment for large scale distributed photovoltaic plant architectures. In *Energy Conversion Congress and Exposition (ECCE), 2011 IEEE*, pages 764–769, Sept 2011.

[20] J.P. Lee, B.D. Min, T.J. Kim, D.W. Yoo, and J.Y. Yoo. High efficient interleaved input-series-output-parallel-connected dc/dc converter for photovoltaic power conditioning system. In *Energy Conversion Congress and Exposition, 2009. ECCE 2009. IEEE*, pages 327–329, Sept 2009.

[21] R.L. Steigerwald. A comparison of half-bridge resonant converter topologies. *Power Electronics, IEEE Transactions on*, 3(2):174–182, Apr 1988.

[22] S Ćuk. A new zero-ripple switching dc-to-dc converter and integrated magnetics. *Magnetics, IEEE Transactions on*, 19(2):57–75, Mar 1983.

[23] D.B. Costa and C.M.C. Duarte. The zvs-pwm active-clamping cuk converter. *Industrial Electronics, IEEE Transactions on*, 51(1):54–60, Feb 2004.

[24] Miao Zhang, Feng Wang, and Jun hua Yang. Novel cuk circuit and its application in photovoltaic system. In *Power Electronics Systems and Applications, 2009. PESA 2009. 3rd International Conference on*, pages 1–4, May 2009.

[25] B. R Lin, C. L Huang, and J. F Wan. Analysis of a zero voltage switching Ćuk converter. In *Industrial Electronics Society, 2007. IECON 2007. 33rd Annual Conference of the IEEE*, pages 1972–1977, Nov 2007.

[26] Zhe Zhang. *Coupled Inductor Magnetics in Power Electronics*. PhD thesis, California Institute of Technology, Pasadena, California, 1987.

[27] Philip Jose. *A Novel ZVS Bidirectional Ćuk Converter with H_∞ Average Current Control for Dual Voltage Systems in Automobiles*. PhD thesis, University of Minnesota, Minneapolis, Minnesota, 2004.

[28] Hariharan Krishnaswami. *Three-port DC-DC Converters to Interface Renewable Energy Sources with Bi-directional Load and Energy Storage Ports*. PhD thesis, University of Minnesota, Minneapolis, Minnesota, 2009.

[29] R.D. Middlebrook and S Ćuk. *Advances in Switched-Mode Power Conversion*, volume I, II, III. Tesla Co., USA, 1983.

[30] D. Maksimovic and R.W. Erickson. *Fundamentals of Power Electronics.* Kluwer Academic Publishers, USA, 2001.

[31] N. Mohan, T. Undeland, and W. Robbins. *Power Electronics: Converters, Applications and Design.* Wiley Academic Publishers, USA, 2002.

[32] John.G. Kassakian, Martin F.Schlecht, and George C.Verghese. *Principles of Power Electronics.* Addison-Wesley Publishers, USA, 1991.

Appendix A

Principle of Duality

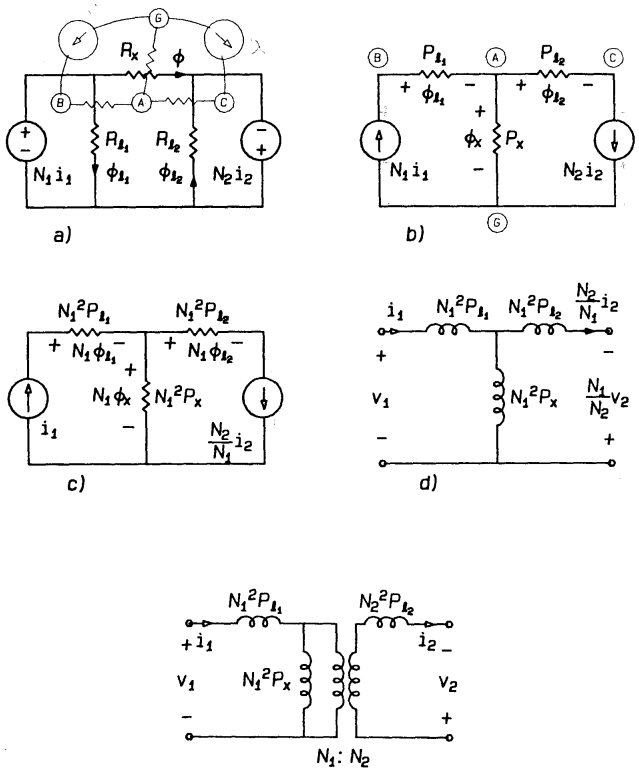

Figure A.1: (a) Finding the Structure of the Dual Circuit (b) The Dual Circuit (c) Scaling the permeances by N^2 (d) The Circuit Model (e) Scaling by an ideal transformer to match the input and output voltages and currents

Appendix B

Typical Leakage Parameter Values

Some leakage parameters for standard cores are mentioned below [26].

Core Type	l (mm)
EI-60(gapped)	2.14
EI-50(gapped)	2.23
EI-40(gapped)	1.60
EI-30(gapped)	1.77
EI-60(spacer)	4.45
EI-50(spacer)	4.60
EI-40(spacer)	3.63
EI-30(spacer)	3.60
EI-22(spacer)	2.40
EI-16(spacer)	1.63
EI-12(spacer)	1.05
EE-60(spacer)	4.41
EE-50(spacer)	4.60
EE-40(spacer)	4.15
EE-30(spacer)	3.49

Continued on next page

Table B.1 – continued from previous page

Core Type	l (mm)
EE-16(spacer)	1.33
EE-13(spacer)	1.30
EE-10/11(spacer)	1.09